Electronic Supplementary Material (ESI) for Green Chemistry.

Supporting Information for

"Revitalizing" Degraded Solid Oxide Fuel Cells in Sour Fuels for Bifunctional Oxygen Catalysis in Zinc-air Battery

Xiaojuan Cao,[a,c†] Ying Yang,[d,c†] Xiaoyu Yan,[a] Norbert J. Geels,[b] Jing-Li Luo [e] and Ning Yan *[abce]

[a] School of Physics and Technology, Wuhan University, Wuhan, China.

[b] Van`t Hoff Institute for Molecular Sciences (HIMS), University of Amsterdam, Amsterdam, The Netherlands.

[c] Suzhou Institute of Wuhan University, Suzhou, China.

[d] Hubei Key Laboratory of Theory and Application of Advanced Materials Mechanics, Wuhan University of Technology, Wuhan, China.

[e] Department of Chemical and Materials Engineering, University of Alberta, Edmonton, Canada.

[†] These authors contribute equally to this work
Corresponding author email address: ning.yan@whu.edu.cn

This file contains

1. Experimental details
2. Supplimentary Tables S1 and S2.
3. Supplimentary Figures S1-S11.

Experimental

1. Fabrication procedures of the SOFC button cell

The anode supported SOFC button cell using Ni-YSZ (8mol% Y doped ZrO_2) as the anode was fabricated via the spin coating method as detailed in our previous work .[1, 2] YSZ and LSM ($La_{0.8}Sr_{0.2}MnO_{3-x}$)-YSZ were employed as the electrolyte and the cathode materials, respectively. Oxygen stream was selected as the cathode oxidant with a flow rate of 50 mL min^{-1}. The anode fuel flow rate was 30 mL min^{-1}. Certified sour gas from *Praxair* (50 ppm $H_2S + H_2$ and 5000 ppm $H_2S + H_2$) was used during the fuel cell test. Gold paste was applied to both sides of the button cell as the current collector while ceramic sealant was applied. At the end of the test, the button cell was rapidly cooled down to room temperature in a stream of 5% $H_2 + N_2$. The averaged cooling rate (non-linear) was approximately 20 ^oC min^{-1}.

2. Degradation and revitalization test of SOFC protocols

The SOFC button cell was mounted between a pair of coaxial alumina tube and heated up to the designated temperature. Then the cell was condition in 5% $H_2 + N_2$ for ~ 30 min till a stable OCV was reached. Another 30 min conditioning was applied in humidified hydrogen before recording the i-V and power density characteristics using a Solartron 1287 electrochemical interface together with a Solartron 1255B frequency response analyzer for the electrochemical impedance spectrum (EIS) measurement. All the spectra were gained at open circuit voltage (OCV) with a frequency range from 0.1 Hz to 100 kHz. In the longevity test, potentiostatic measurement was carried out via biasing the cell at 0.8 V at 850 ^oC in a stream of sour fuel (50 ppm $H_2S + H_2$).

After the degradation test, the fuel stream to the anode was switched to 5000 ppm $H_2S + H_2$ at 850 ^oC and OCV condition. This sulfidation process took 5 min before switching the fuel back to 5% $H_2 + N_2$ and cooling down to room temperature. Then all the ceramic sealant, gold current collector, LSM cathode layer and the dense YSZ electrolyte layer were removed using sand paper. The resulting anode functional layer and the think support was crushed into small pieces (shard catalyst, length < 3mm) manually using a hammer. The powder catalyst was obtained by further processing the shard catalyst using a pulverizer (Fritsch, pulverisette 2) equipped with ZrO_2 grinding tools, followed by the sieving using a 500-mesh sieve. The resulting particle size is less than 25 μm (typical size is 10~20 μm).

3. Oxygen bifunctional catalysis test protocols

The ORR catalytic properties were evaluated using a rotating disk electrode (RDE). Catalyst inks were prepared by suspending 4 mg NiS_x/YSZ and 1 mg of commercial carbon black (CB) in 1 mL ethanol and 10 μL Nafion® (D-521 dispersion 5 wt.% in water/isopropanol), and sonicated overnight. The obtained catalyst was denoted as NiS_x/YSZ-CB. The working electrode tip (glassy carbon disk 0.196 cm^{-2}) was polished with diamond polishing film containing 0.1 μm particles and rinsed with water afterwards. The working electrode was prepared by drop casting 6 × 5 μL ink, while air drying between casts. 20 wt.% Pt and 5 wt.% Ru on carbon was used for comparison.

The number of electrons transferred in the reaction was estimated by the Koutecký-Levich equation:

$$\frac{1}{J} = \frac{1}{B\omega^{-1/2}} + \frac{1}{J_K}$$

Where J is the measured current density (mA cm^{-2}), JK is the kinetic (exchange) current density (mA cm^{-2}), ω is the RDE rotation rate (rpm), and B is given by:

$$B = 0.2nFC_O D_O^{2/3} \nu^{-1/6}$$

Where 0.2 is the arithmetic correction factor for ω in rpm, n is the number of electrons transferred per mol, F is Faraday's constant, C_O is the concentration of dissolved O_2 (1.2 mmol ml^{-1} at 25 °C in 0.1 M KOH), D_O is the diffusion coefficient of O_2 ($1.9 \cdot 10^{-5}$ cm^2 s^{-1} at 25 °C in 0.1 M KOH), and υ is the kinematic viscosity of the 0.1 M KOH electrolyte at 25 °C (0.01 cm^2 s^{-1}). By plotting 1/J versus $\omega^{-1/2}$ at different potentials and fitting linear equations to the data, the number of electrons (n) could be calculated from the slope (1/B).

The OER catalytic properties evaluation was also carried out using the 3-electrode setup. The work electrode was prepared by dispersing powder and shard NiS_x/YSZ on a piece of Ni sheet covered with Au paste as the adhesive. The catalyst loading for was *ca.* 7.5 mg cm^{-2} and 1.0 mg cm^{-2} for shard and powder catalyst, respectively. Then the electrode was dried in an oven at 70 ^{o}C for 30 min. Ni sheet only with Au cover was also tested as a reference. The active area of the electrode was 0.25 cm^{-2} (1 cm × 0.25 cm). The stability test was carried out using a two-electrode setup in overall water splitting reaction. The Ni sheet with the electrodeposited Pt catalyst was used as the cathode catalyst. The chronoamperometric measurement was performed via biasing the cell at 1.53 V (η =300 mV).

Electrochemical experiments were performed using a Gamry Reference 600 potentiostat. All electrochemical experiments were performed at 25 °C in 0.1 M KOH aqueous electrolyte. A saturated calomel electrode (SCE) was used as a reference electrode, separated from the solution with a luggin capillary. Potentials were reported vs RHE by adding 1.006 V (pH = 13) to the measured SCE potential. A graphite rod was used as a counter electrode, presoaked with the electrolyte 24 hours prior to the measurements. Oxygen was bubbled through the solution for a minimum of 30 min, where after the gas was flown over the solution (gas blanket). EIS spectra were recorded at η =300 mV. Prior to the experiment, the solution resistance was measured and 95% of this value was used as a positive correction factor in post measurement iR drop correction. Before measurements, cyclic voltammograms were recorded from 0.3 to 1.0 V vs RHE till no change in current was observed.

4. Zn-air battery assembly and test procedures

A rechargeable liquid Zn-air battery was assembled using a homemade test cell. The anode was made of a polished Zn plate (0.5mm) and the electrolyte was the aqueous solution containing 6 M KOH and 0.2 M $ZnCl_2$. The cathode comprised a hydrophobic piece of carbon cloth sandwiched by a gas diffusion layer and a catalyst layer. The latter was fabricated by drop-casting the NiS_x/YSZ-CB catalyst ink on the cloth. As the control, a mixture of 20 wt.% Pt and 5 wt.% Ru on carbon (mass ratio was 1:1) was also used as the catalyst layer. The Gamry Reference 600 potentiostat was used in the electrochemical measurement. The discharging i-V and power density characteristics were recorded at the scan rate of 50 mV s^{-1}. The cyclic charging-discharging test was performed at a current density of 10 mA cm^{-2}. Both the charging and discharging cycle was set at 20 min, between which the 10 min rest time was applied.

5. Simulation procedures

The Vienna *ab initio* Simulation Package (VASP)[3-5] was used to perform the density-functional theory (DFT) calculation. The slab models of all the examined stable nickel sulfides, including NiS, Ni_3S_2, Ni_3S_4 and Ni_9S_8, is comprised of four atomic layers. The vacuum layer was 20 Å thick. The low-index cleavage planes, which were (111), (100), and (110), were adopted as reported elsewhere.[6-9] The slab geometry optimization was performed, allowing half of the bottom atomic layers constrained while other layers being relaxed, till the force components were less than 0.05 eV/Å. The Monkhorst-Pack k-point was obtained using a 6×6×1 mesh. The binding energies of all the oxygen intermediates were calculated under standard conditions.

6. Materials characterizations

X-Ray diffraction (XRD) patterns were obtained using a MiniFlex II diffractometer equipped with CuKα radiation. The X-ray tube was operated at 30 kV and a current of 5 mA. Mercury intrusion porosimetry was performed on a Ce Instruments Pascal 440 measuring up to 400 MPa. Before analysis, the samples were dried in vacuum ($1 \cdot 10^{-3}$ mbar) at 200 °C for 3 h. The microstructural morphologies were examined in both planar and cross-sectional views using a Zeiss EVO electron microscope (SEM) equipped with a Bruker silicon drift detector for the acquisition of elemental and energy dispersive x-ray (EDX) mapping information. Transmission electron microscope (TEM) analysis was performed using a Talos F200S field emission transmission electron microscope. X-ray photoelectron spectroscopy (XPS) was carried out using a Kratos AXIS equipped with a monochromatic Al Kα X-ray source. The base pressure in the analytical chamber was maintained below 10^{-9} mbar. The obtained spectra were analyzed using the Thermo Avantage software calibrated to the C 1s binding energy of 284.5 eV. For curve fitting and deconvolution, a Shirley-type background subtraction and a Gaussian-Lorentzian peak shape were applied.

Table S1. Comparison of the OER activities of NiS_x/YSZ on nickel sheet with selected high-performance electrocatalysts in alkaline media.

Catalyst	**$\eta_{=10}$ (mV)**	**pH**	**References**
Co_9S_8/N-graphene	410	13	*Energ. Environ. Sci.*, 2016, 9, 1320-1326
NiFe@NC	360	14	Nano Energy .2017, 39, 245–252
p-SnNiFe	350	14	Nat. Commun. 2017, 8, 934
CoMnP	330	14	J. Am. Chem. Soc. 2016, 138, 4006-4009
Co_4N	330	14	J. Am. Chem. Soc. 2015, 137, 4119-4125
Poled Co2	320	14	Nat. Commun. 2016, 8, 14430
$CoSe_{0.85}$	300	14	Adv. Mater. 2016, 28, 77-85
CoFe LDH-F	300	14	Adv. Mater. Interfaces. 2019, 10, 1409
boronized Ni	300	14	J. Mater. Chem. A, 2019, 7, 5288-5294
CoFe LDH/NF	300	14	ChemPlusChem 2017, 82, 483
$SCFW_{0.4}$	296	14	J. Mater. Chem. A 2018, 6, 9854-9859
α-$Co_4Fe(OH)x$	295	14	J. Mater. Chem. A 2017, 5, 1078
Ni_3S_2	295	14	Nanoscale, 2019, 11, 5646-5654.
Zn doped CoO	293	14	ChemCatChem 2019, 11, 1480–1486
CoM-P-3DHFLMs	292	14	Appl. Catal., B 2019, 249 147–154
Amorphous CoSe film	292	14	Chem. Commun. 2015, 51, 16683-16686
Ni_3N nanosheets	290	14	Angew. Chem. Int. Ed. 2016, 55, 8670-8674
Ni_2P	290	14	Energy Environ. Sci. 2015, 8, 2347-2351.
Co-Bi NS/G nanosheets	290	14	Angew. Chem. Int. Ed. 2016, 55, 2488
NiS_x/YSZ	290	13	This work
p-$Cu_{1-x}NNi_{3-y}$/FeNiCu	280	14	Nat. Commun. 2018, 9, 2326

Note: Most OER catalysts in alkaline media were tested at pH 14.

Table S2. Performance of selected excellent oxygen bifunctional catalyst in alkaline condition (pH =13) reported recently.

Catalyst	**E_{OER-10} (V)** [a]	**$E_{ORR-1/2}$ (V)** [b]	**ΔE (V)**[c]	**Reference**
Pt/C	1.90	0.91	0.99	This work
RuO_2/C	1.64	0.69	0.95	This work
N-Co9S8/G	1.64	0.704	0.936	Energy Environ. Sci. 2016, 9, 1320-326.
Fe@C-NG/NCNTs	1.68	0.84	0.84	J. Mater. Chem. A, 2018, 6, 516-526.
MnCo2O4	1.61	0.74	0.83	Angew. Chem., Int. Ed. 2017, 56, 14977-14981.
NC@Co-NGG DSNCs	1.64	0.82	0.82	Adv. Mater. 2017, 29, 1700874.
Co–Nx/CNRA	1.69	0.9	0.79	Adv. Funct. Mater. 2018, 28, 1705048.
AlFeCoNiCr	1.47	0.71	0.76	Appl. Catal. B, 2019, in press, DOI: 10.1016/j.apcatb.2019.118431
Co_3O_4/N-p MCNTs	1.62	0.86	0.76	ACS Appl. Energy Mater., 2019, 2, 4428-4438.
Co/S/N-800	1.591	0.831	0.76	ChemSusChem, 2019, 12, 3390-3400.
GNCNTs-4	1.6	0.85	0.75	Adv. Funct. Mater., 2020, 30, 1906081.
CoP-DC	1.55	0.81	0.74	Adv. Energy Mater., 2018, 8, 1703623.
NiS_x/YSZ-CB	1.56	0.82	0.74	This work

Note:

[a]: OER potential at the benchmark 10 mA cm^{-2}.

[b]: half-wave potential of ORR

[c]: $\Delta E = E_{OER-10} - E_{ORR-1/2}$.

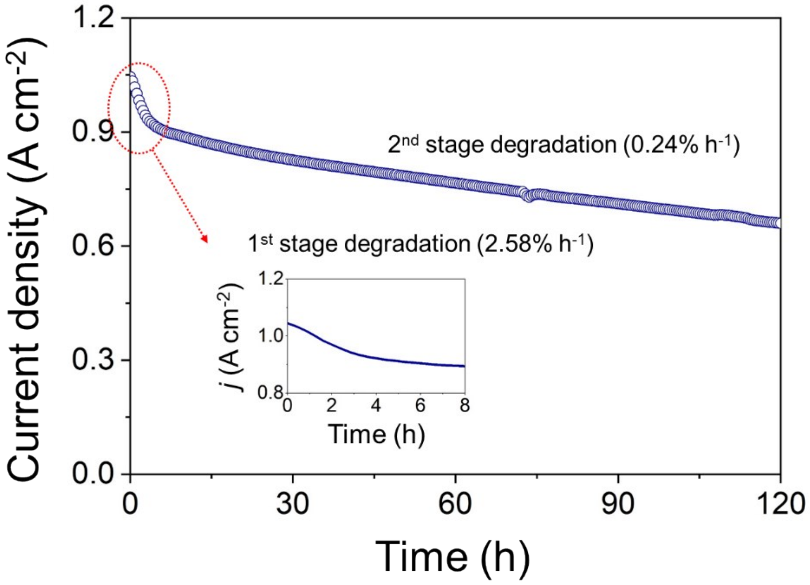

Figure S1. Long-term potentiostatic operation of the SOFC button cell in 50 ppm H_2S + H_2 at 850 °C. The potential bias is 0.8 V; degradation rate per hour in different stages is listed in the parentheses.

This is a simulated and accelerated degradation test of SOFC fed by fuels with sulfur containing odorant. The first stage degradation was rapid which lasted for ~4 h, pertaining to the poisoning of the nickel anode. In the second stage, the current declined slowly, suggesting that a saturated poisoning state might be reached.

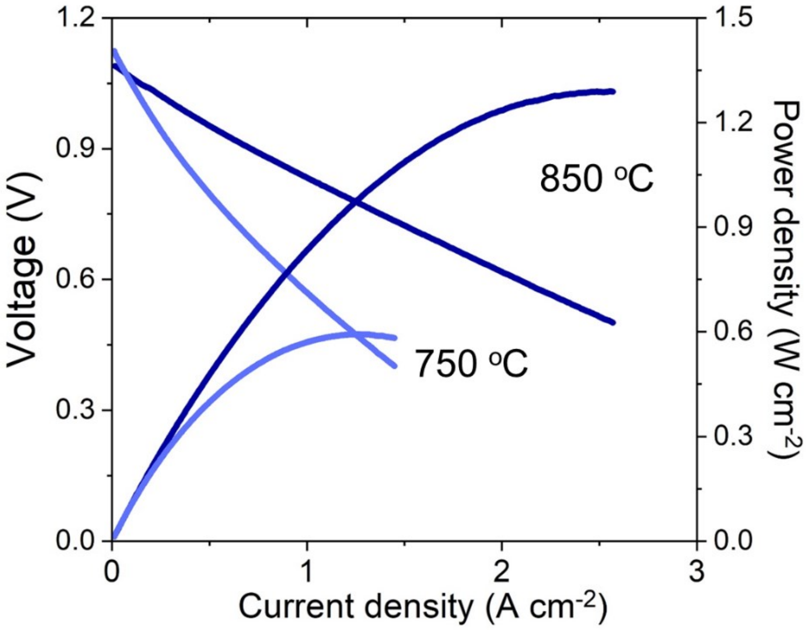

Figure S2. The i-V and power density profiles of fresh SOFC in H_2 recorded at 750 ^{o}C and 850 ^{o}C, respectively.

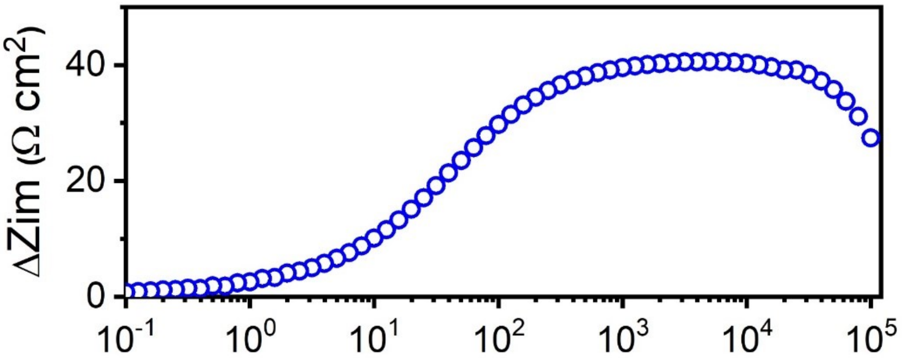

Figure S3. The delta Bode plot of the EIS spectra recorded in H_2 at 850 °C between fresh SOFC and revitalized SOFC after 5 min 5000 ppm $H_2S + H_2$ sulfidation treatment at 850 °C.

Here in the ΔZim plots, the spectrum of fresh SOFC in H_2 was used as the baseline from which the impedance spectra of the revitalized SOFC was simply subtracted. It could be seen that the revitalized process in sour fuel gave rise to a change of the high frequency region at a summit of around $10^3 \sim 10^4$ Hz which was usually assigned to the anode process, whereas the low frequency region, associated with the mass transfer and cathodic process, was not affected ($\Delta Z_{im} \approx 0$).

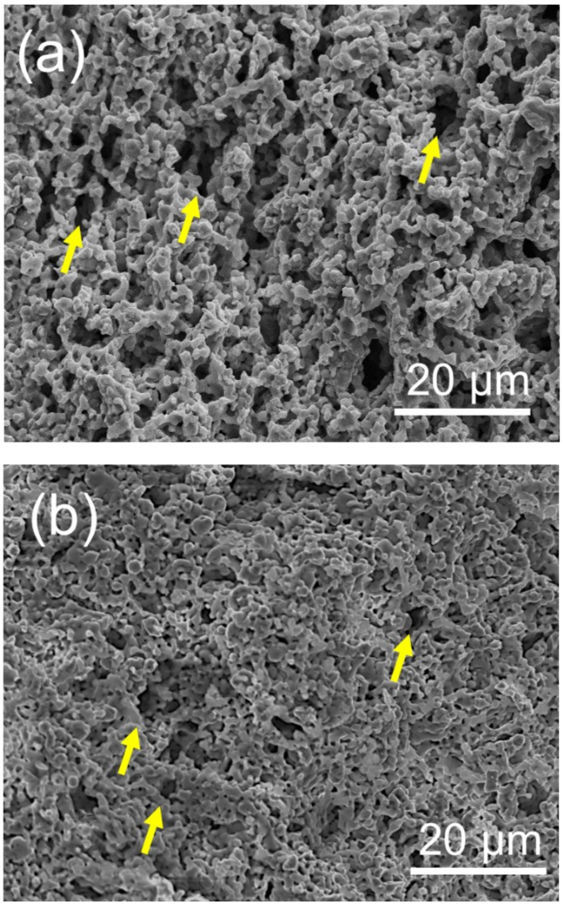

Figure S4. The cross-sectional SEM images of the SOFC anode (a) before and (b) after the revitalization treatment.

The arrows indicate that the large pores (~ 10 μm) created by the corn-stack pore in the fresh SOFC anode have been partially filled up as the eutectic liquid has high mobility. While this has decreased the portion of these large pores, the average pore size of the treated anode has significantly increased as proven by the mercury intrusion porosimetry.

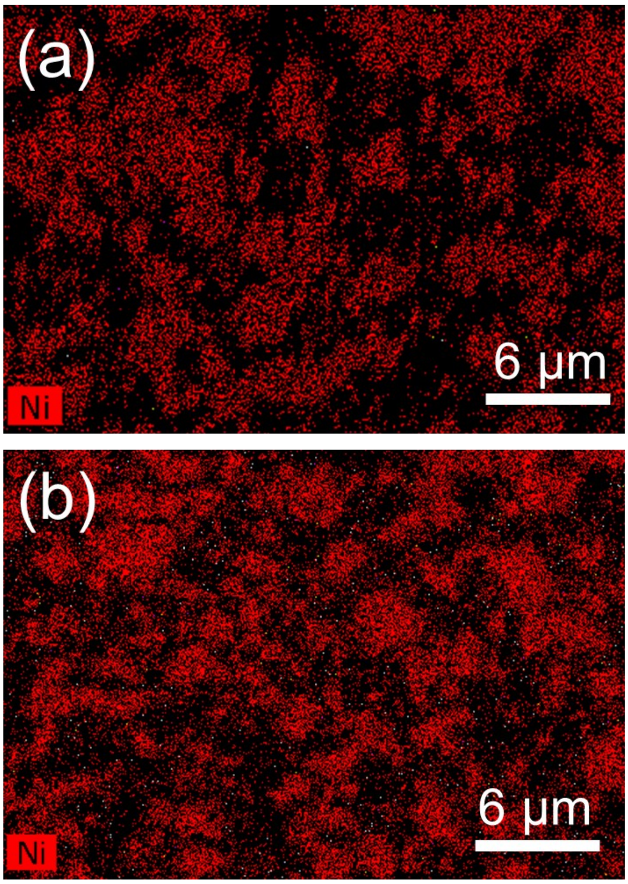

Figure S5. The cross-sectional SEM-EDX elemental mapping of Ni in the SOFC anode (a) before and (b) after the revitalization treatment.

Redistribution of Ni-containing compounds is noticeable. While this partially impaired the electronic percolation, the redistribution yet decreased the particle size of Ni species and optimized the porous structure.

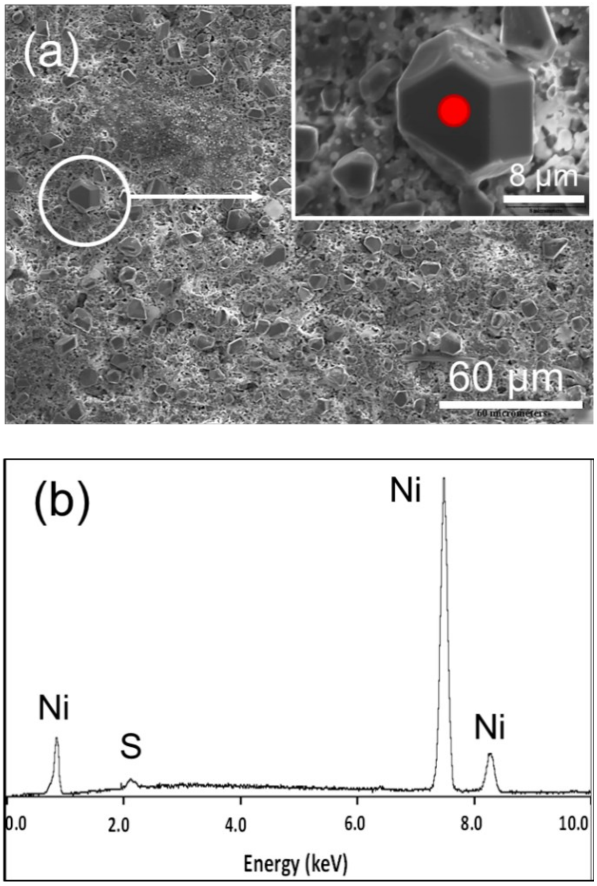

Figure S6. (a) The SEM image of the SOFC anode surface; the inset is the magnified image of a nickel-sulfur crystal formed during the revitalization process; (b) the EDX spectrum of the red spot in (a).

The formation of Ni-S crystal on the surface of SOFC anode was resulted from the redistribution of Ni species during the sulfidation process. This large crystal is an even clearer evidence showing the presence of liquid phase in the sulfidation process.

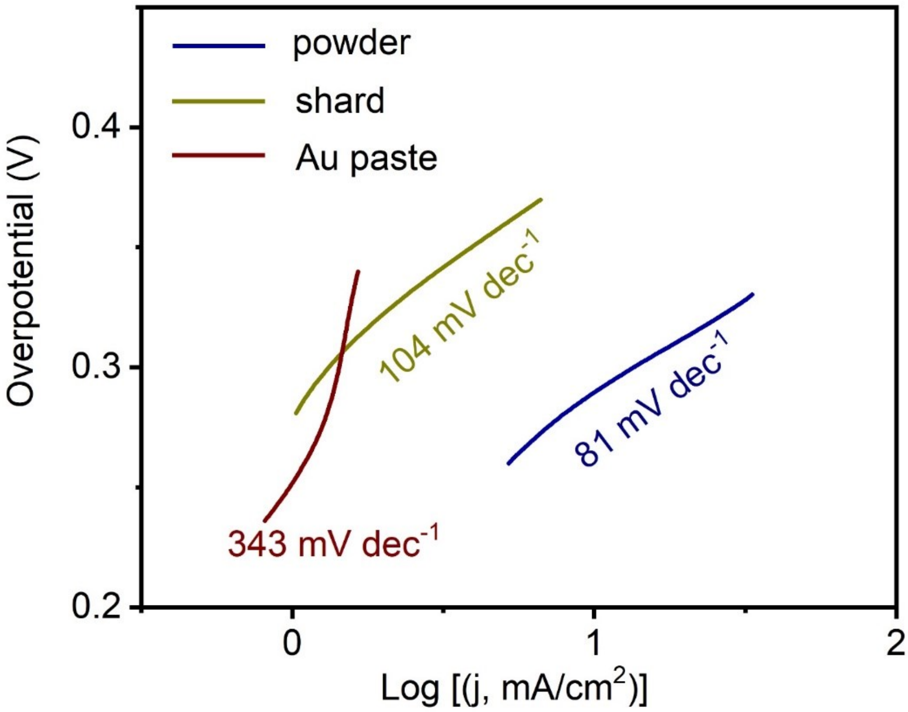

Figure S7. Comparison of the Tafel plots of various materials in OER at pH 13.

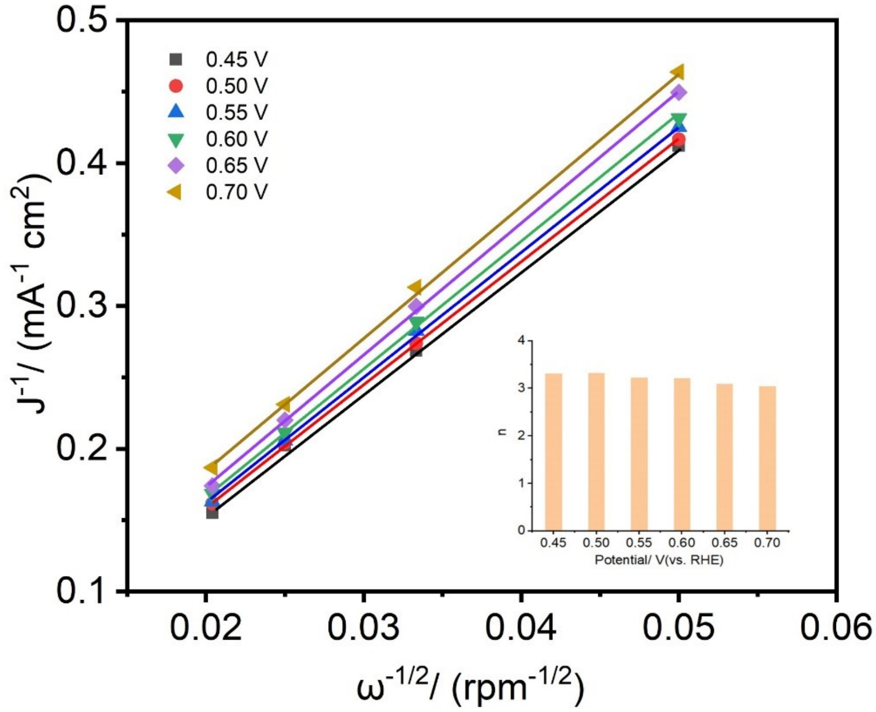

Figure S8. The Koutecký-Levich plots of NiS_x/YSZ-CB at various potentials; the inset shows the plots of the number of the electron transfer.

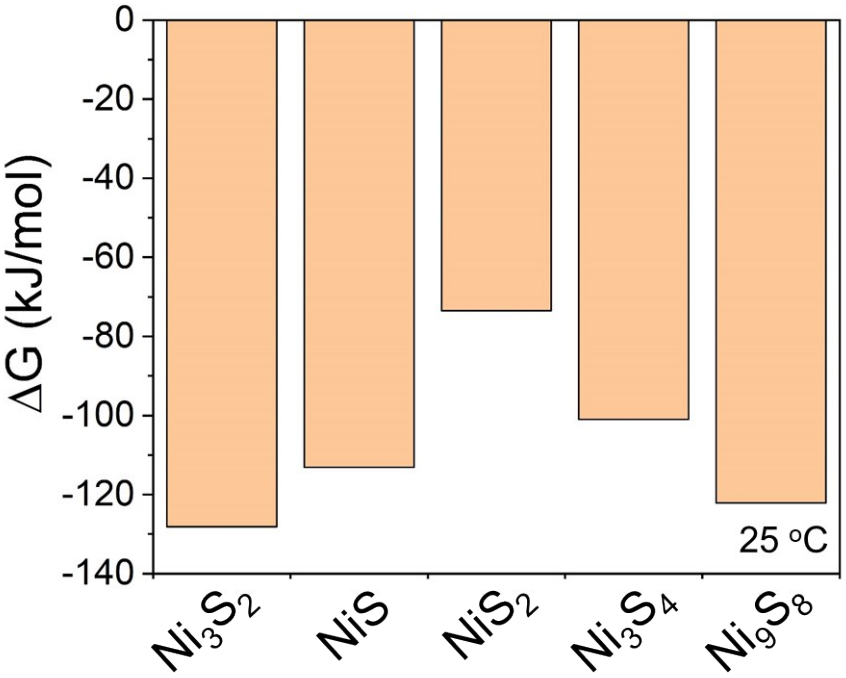

Figure S9. The change of the the Gibbs free energy (ΔG) of the NiOOH-formation reaction starting from various nickel sulfides at the standard conditions assuming 1 mole of NiOOH is formed.

The reactions are listed below:

[1] $0.75O_2(g) + 0.33Ni_3S_2 + 0.5H_2O(l) = NiOOH + 0.67S$

[2] $0.75O_2(g) + NiS + 0.5H_2O(l) = NiOOH + S$

[3] $0.75O_2(g) + NiS_2 + 0.5H_2O(l) = NiOOH + 2S$

[4] $0.75O_2(g) + 0.33Ni_3S_4 + 0.5H_2O(l) = NiOOH + 1.33S$

[5] $0.75O_2(g) + 0.11Ni_9S_8 + 0.5H_2O(l) = NiOOH + 0.89S$

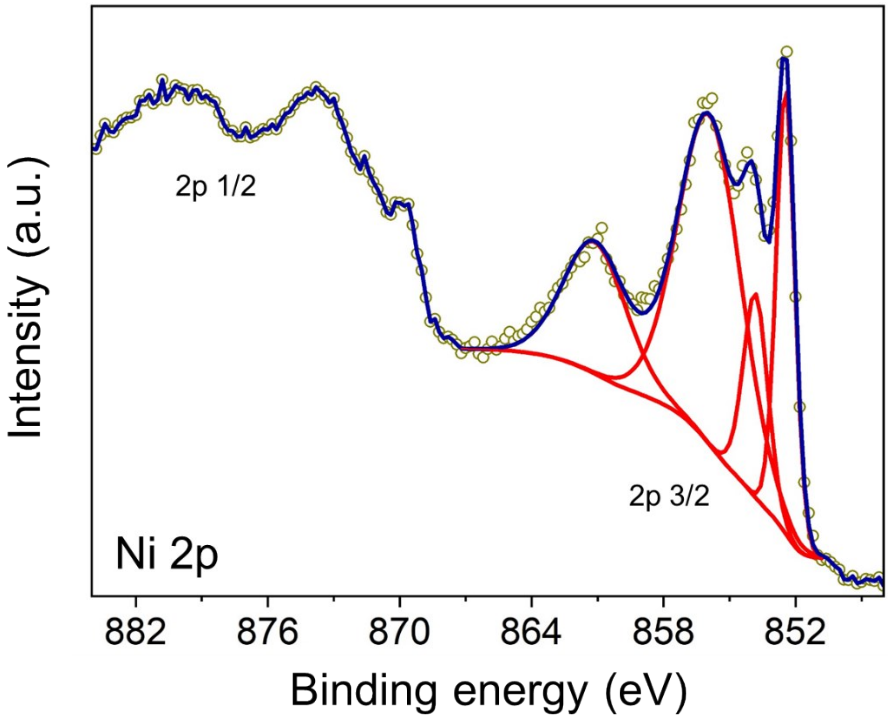

Figure S10. The high-resolution XPS spectrum at Ni 2p core level of the spent NiS_x/YSZ-CB catalyst.

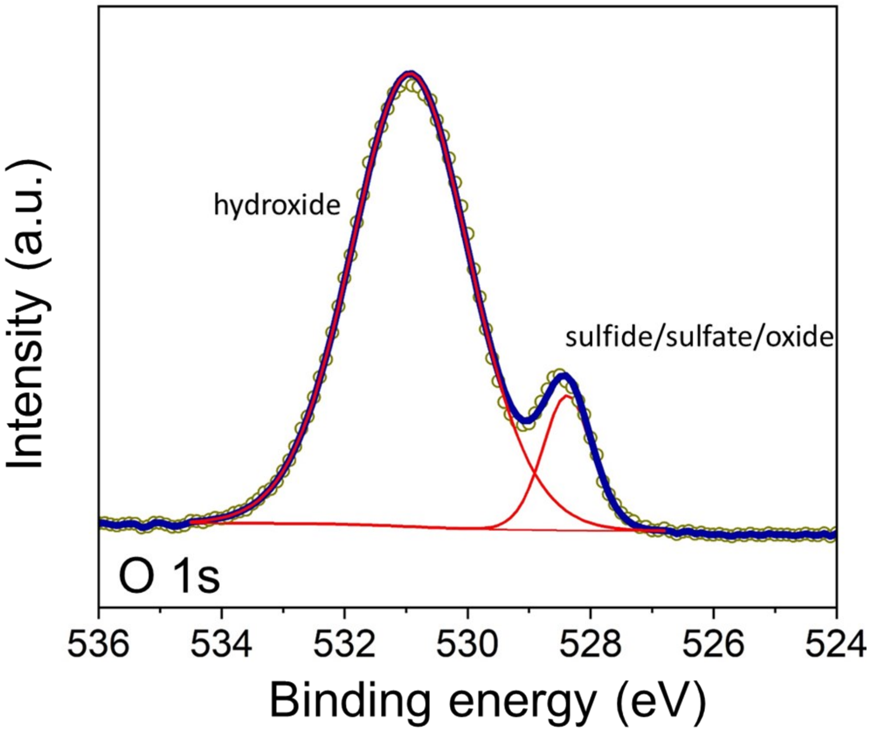

Figure S11. The high-resolution XPS spectrum at O 1s core level of the spent NiS_x/YSZ-CB catalyst.

References

[S1] N. Yan, X. Z. Fu, J. L. Luo, K. T. Chuang, A. R. Sanger, *J. Power Sources*, 2012, **198**, 164-169.

[S2] N. Yan, J. L. Luo, K. T. Chuang, *J. Power Sources*, 2014, **250**, 212-219.

[S3] G. Kresse and J. Hafner, *Physical Review B*, 1994, **49**, 14251-14269.

[S4] G. Kresse and J. Furthmuller, *Computational Materials Science*, 1996, **6**, 15-50.

[S5] G. Kresse and J. Furthmuller, *Physical Review B*, 1996, **54**, 11169-11186.

[S6] B. Yan, D. Krishnamurthy, C. H. Hendon, S. Deshpande, Y. Surendranath and V. Viswanathan, *Joule*, 2017, **1**, 600-612.

[S7] Z. Zheng, T. Su, J. P. Shi, R. Tong, H. B. Xiao, Q. Zhang, Y. F. Zhang, Z. Wang, Q. Li and X. N. Wang, *Nanoscale*, 2019, **11**, 22971-22979.

[S8] X. R. Zheng, X. P. Han, Y. Q. Zhang, J. H. Wang, C. Zhong, Y. D. Deng and W. B. Hu, *Nanoscale*, 2019, **11**, 5646-5654.

[S9] J. Y. Zhang, X. W. Bai, T. T. Wang, W. Xiao, P. X. Xi, J. L. Wang, D. Q. Gao and J. Wang, *Nano-Micro Letters*, 2019, **11**.